

Sparse Deformable Models with Application to Cardiac Motion Analysis

Yang Yu¹, Shaoting Zhang^{1,*}, Junzhou Huang²,
Dimitris Metaxas¹, and Leon Axel³

¹ Department of Computer Science, Rutgers University, Piscataway, NJ, USA

² Computer Science and Engineering, University of Texas at Arlington, TX, USA

³ Radiology Department, New York University, New York, NY, USA

shaoting@cs.rutgers.edu

Abstract. Deformable models have been widely used with success in medical image analysis. They combine bottom-up information derived from image appearance cues, with top-down shape-based constraints within a physics-based formulation. However, in many real world problems the observations extracted from the image data often contain gross errors, which adversely affect the deformation accuracy. To alleviate this issue, we introduce a new family of deformable models that are inspired from compressed sensing, a technique for efficiently reconstructing a signal based on its sparseness in some domain. In this problem, we employ sparsity to represent the outliers or gross errors, and combine it seamlessly with deformable models. The proposed new formulation is applied to the analysis of cardiac motion, using tagged magnetic resonance imaging (tMRI), where the automated tagging line tracking results are very noisy due to the poor image quality. Our new deformable models track the heart motion robustly, and the resulting strains are consistent with those calculated from manual labels.

1 Introduction

Deformable models have been widely used in computer vision [8], computer graphics [10] and medical image analysis [7]. They are able to solve diverse types of problems, such as, but not limited to, image segmentation [6], shape reconstruction [16], and motion tracking [11]. The name “deformable models” is derived from nonrigid body mechanics, which describes how elastic objects respond to applied forces. Starting from an initial shape, the model is deformed by two types of forces, i.e., internal and external forces. The internal forces limit the geometric flexibility of the shape, while the external forces drive the model to fit the observations. For example, in the initial active contour models [6], the internal forces are based on the first-order and second-order shape terms of the boundary. They regularize the length and the curvature of the underlying shape, to ensure a smooth shape result. The external forces drag the boundary to the positions that are more likely to be

* Corresponding author.

edges. Because of the success of the active contours, many methods have been proposed since then to improve the performance of deformable models by modifying either the internal or external forces.

The internal forces usually enforce the smoothness characteristics of deformable models, such as the local continuity and curvature. 2D or 3D splines are widely used to constrain the image deformation [1]. B-spline [12] and nonuniform rational B-splines (NURBS) [17] define the model motion inside the object and on the boundary. They effectively reduce the degree of freedom for deformation and regularize the curvature on the deformation field. The Laplacian coordinate [15] is another well-known measurement for the local relative positions. Comparing with spline-based method, methods based on Laplacian coordinate allow more flexible shape representation. Sorkine et al. employed it to constrain the smoothness and local similarity of the 2D mesh deformation in geometry editing [15]. Shen et al. [14] decomposed the Laplacian coordinates into components in the perpendicular and tangential directions of the model, to formulate a detail-preserved internal force. Since the component of the perpendicular direction tends to shrink the model and eliminates the shape details, they proposed an internal force based on the tangential direction, to better approach the sharp features. In this paper, we apply the Laplacian coordinates on 3D volume models to enforce the smoothness not only on the surface, but also inside the models.

The external forces usually drive the model based on the control points extracted from low-level image information [13]. However, their positions may not be accurate, due to the noisy and/or weak image appearance cues. A general strategy to apply the external force is to minimize the distances between the control points extracted from image and the corresponding points on the initial model [15,20]. They used a Euclidean distance or $L2$ norm to measure the differences between the observations and the corresponding model control points. This assumes intrinsically that the errors of the control points follow a Gaussian distribution. Nevertheless, this is not always true in practice. They may contain not only Gaussian noise, but also some gross errors or outliers due to the erroneous tracking. Therefore, the accuracy of the traditional deformable models depends heavily on the control point accuracy. To improve the robustness of deformable models, Vogler et al. [18] explicitly modeled the distribution of control points, and considered the points rejected by the distribution as outliers. The local tracking results were first projected to the parameter space. Then they estimated a normal distribution based on the observations and rejected that with large Mahalanobis distance to the mean. Different from [18], our proposed deformable models implicitly handle the outliers with no elimination step. The influence of each local tracking observations is adaptively decided during the optimization process. The models are general enough for arbitrary deformable models with gross errors in the observations.

Inspired by the robust recovery power of the compressed sensing approach [3], we propose a new class of deformable models using sparse constraints. Recent research in compressed sensing shows that using an $L1$ norm can dramatically increase the probability of accurate signal recovery, even when there are both

sparse outliers and moderate Gaussian noise [3]. Thus, we first propose a deformable model with only a $L1$ norm constraint, which is able to handle outliers robustly. However, when the variances of the Gaussian noise are large, solely using the $L1$ norm will cause overfitting problems because of its nature of pursuing the sparse structure [3]. Therefore, we further propose a deformable model using a hybrid norm constraint able to handle both the Gaussian errors and gross errors. We also generalize these two models in a unified formulation, named as Sparse Deformable Models. We apply the models to left ventricle (LV) motion analysis on mouse cardiac tagged MRI. The experiment results show that we can robustly track the mouse heart motions even based on inaccurate control point tracking results.

2 Methodology

Consider a set of points \mathcal{V} , where each point has a neighborhood structure¹, and a subset as control points \mathcal{V}_c that are computed from the observations (e.g., image information). Let the homogeneous coordinate of the point i be denoted by $\mathbf{v}_i = [x_i, y_i, z_i, 1]^T$ and the position after deformation $\mathbf{v}'_i = [x'_i, y'_i, z'_i]^T$, where $i = 1, 2, \dots, n$. We denote the coordinates of all the points after deformation as:

$$\mathbf{V}' = [\mathbf{v}'_1^T \mathbf{v}'_2^T \cdots \mathbf{v}'_n^T]^T.$$

The goal of our deformable models is to track the motion of the whole shape, given a set of control points. The deformation of each point i is parameterized by an affine 3×4 transformation matrix T_i . The unknown transformation parameters are organized in a $4n \times 3$ matrix:

$$T = [T_1 T_2 \cdots T_n]^T.$$

In our model, the internal forces preserve the local shape structure with the Laplacian coordinate, and the external forces minimize the difference between the shape and the control points with our proposed sparse constraints.

2.1 Internal Force

Our internal force ensures that the deformation matrices are similar among the neighborhood points. The similarity is measured based on the deformation they generate. Specifically, if we apply transformation matrices of neighboring points to the current one, the resulting displacements should be similar. For a point i , its displacement after applying its own transformation matrix T_i should be similar to applying its neighbor's transformation matrix T_j . Thus, the energy function of the internal force is:

$$E_{int} = \sum_{i \in \mathcal{V}} \sum_{j \in \mathcal{N}(i)} w_{ij} \|T_i \mathbf{v}_i - T_j \mathbf{v}_i\|_2^2, \quad (1)$$

¹ Mesh and meshless-based models are the most widely used shape representations. Our model works for both representations, and the neighborhood is defined by the connectivity for the mesh model, or the distance for the meshless model.

where $\|\cdot\|_2$ denotes the entry-wise matrix $L2$ norm², and weight w_{ij} is related to the distance between points i and j . Since this is a summation of the quadratic forms of the transformation matrices T_i , we can represent the energy function as a quadratic form of all the unknown transformations T . To do so, the point position \mathbf{v}_i is encoded into matrix K_i as

$$K_i = M_i \otimes \mathbf{v}_i,$$

where \otimes is the Kronecker product, and M_i is a $m_i \times n$ node-arc matrix of \mathbf{v}_i , where m_i is the number of its neighbors. For each neighbor \mathbf{v}_j , there is one row in M_i where the i th element is w_{ij} and the j th element is $-w_{ij}$, while the other elements are all zeros:

$$M_i = \begin{pmatrix} \cdots & \overset{\text{ith column}}{w_{ij}} & \cdots & \overset{\text{jth column}}{-w_{ij}} & \cdots \\ & \vdots & & \vdots & \end{pmatrix}, j \in \mathcal{N}(\mathbf{v}_i).$$

$K_i T$ is the difference of the displacements based on different transformations of the neighborhood of point i . We concatenate the matrix K_i for all the points to form the matrix $K = [K_1^T K_2^T \cdots K_n^T]^T$. Thus, the energy function of the internal force (Eq.1) is formulated as:

$$E_{int} = \|KT\|_2^2. \quad (2)$$

2.2 External Force

Besides the shape constraint from the internal force, the deformable model also aims to match the observations. For example, a point i on the model is expected to fit to the given control point position \mathbf{v}'_i after deformation T_i . We concatenate the point coordinates into an $n \times 4n$ sparse matrix:

$$D = \begin{bmatrix} \mathbf{v}_1^T & & & \\ & \mathbf{v}_2^T & & \\ & & \ddots & \\ & & & \mathbf{v}_n^T \end{bmatrix},$$

where $\mathbf{V}' = DT$ is the model deformation based on the transformation parameters T . We use a control point indicator c to select the rows of D and \mathbf{V}' corresponding to the control points. Thus, the Laplacian deformable model (LDM) is defined as:

$$\arg \min_T \{ \|KT\|_2^2 + \lambda \|D_c T - \mathbf{V}'_c\|_2^2 \}, \quad (3)$$

where λ is the stiffness weight, which controls how much the model is able to deform to match the control points. Larger λ results in a better fitting, but the

² The matrix norms in the paper are all entry-wise norms.

deformed shape may not be smooth. The $L2$ norm is used as a penalty function in this formulation. As the standard norm on the Euclidean space, the $L2$ norm is the most widely used distance metric. However, it may not be the most proper metric in some applications, especially when there are gross errors or outliers.

The Sparse Prior Using $L1$ Norm. Gross errors are very common in some applications, such as the erroneous detections in a noisy image. The $L2$ norm follows a Gaussian distribution for residuals. It may overfit these sparse outliers, and hence reduce the deformation accuracy. It is desirable to produce a sparse solution that models the outliers. The $L0$ norm counts the number of non-zero elements and can model such sparse errors exactly. However, the $L0$ norm is non-convex, and solving an $L0$ norm problem is NP-hard. Recent developments in compressed sensing [3] show that minimizing an $L1$ norm problem can produce a nearly identical solution as using the $L0$ norm. Thus, we use convex relaxation to define a sparse deformable model based on the $L1$ norm as:

$$\arg \min_T \{ \|KT\|_2^2 + \lambda \|D_c T - \mathbf{V}'_c\|_1 \}. \quad (4)$$

The Sparse Prior Using Both $L1$ and $L2$ Norms. The sparsity constraint is useful in many applications, such as signal reconstruction and background subtraction. However, in most cases, the observations may still contain Gaussian errors with large variations. Using the $L1$ norm alone may not be able to handle them well [23]. Therefore, we combine both $L1$ and $L2$ norms and propose our sparse deformable models for general problems:

$$\arg \min_{T, \mathbf{e}} \{ \|KT\|_2^2 + \lambda (\|D_c T - \mathbf{V}'_c - \mathbf{e}\|_2^2 + \gamma \|\mathbf{e}\|_1) \}, \quad (5)$$

where \mathbf{e} represents the gross errors and is constrained by the $L1$ norm, and $\gamma \in [0, 1]$ controls how sparse \mathbf{e} is. The new model combines the advantages of both $L1$ and $L2$ norms. If γ is extremely large, \mathbf{e} will be all zeros. Thus the model degenerates to a method with only an $L2$ norm, as in (3). It will be sensitive to any gross errors. If λ is extremely large and γ is small, the deformation errors will be approximately equal to \mathbf{e} . Thus the model is similar to models with only sparse constraints, as in (4). It will be robust to the outliers, but can not handle large Gaussian noise.

Optimization Framework. The above problem can be solved by the standard convex optimization algorithm, while we propose an effective iterative optimization algorithm that fully utilizes the special structure of the problem. The two variables T and \mathbf{e} are optimized alternatively, with an analytical solution. The gross error \mathbf{e} is initialized as zero. When \mathbf{e} is fixed, the problem is reduced to the conventional $L2$ norm constraints.

$$\arg \min_T \{ \|KT\|_2^2 + \lambda \|D_c T - \mathbf{V}'_c - \mathbf{e}\|_2^2 \}, \quad (6)$$

It can be solved by least square minimization. Then T is fixed, and the optimization problems for each term e_i of the outlier \mathbf{e} are independent:

$$\arg \min_{e_i} \{((D_c T)_i - \mathbf{V}'_{ci} - e_i)^2 + \gamma|e_i|\}, \quad (7)$$

where $(D_c T)_i$ is the i th element of the vector $D_c T$. The minimums for the two parts can be achieved at $(D_c T)_i - \mathbf{V}'_{ci}$ and 0 separately. Since both of them are convex, the minimum of the energy function must lie between them. Therefore, e_i has the same sign as $(D_c T)_i - \mathbf{V}'_{ci}$. After determining the sign of e_i , the problem reduces to a constrained quadratic function of e_i . The solution is:

$$e_i = \begin{cases} \max\{0, (D_c T)_i - \mathbf{V}'_{ci} - \gamma/2\} & \text{if } (D_c T)_i - \mathbf{V}'_{ci} \geq 0, \\ \min\{0, (D_c T)_i - \mathbf{V}'_{ci} + \gamma/2\} & \text{otherwise.} \end{cases} \quad (8)$$

The analytical solutions of the two sub-steps guarantee the energy monotonically decreases until the minimum is achieved. The convexity of the whole problem makes sure that this is the global solution of the problem.

2.3 Left Ventricle Motion Analysis

Tagged MRI (tMRI) offers a powerful non-invasive tool for making measurements of the beating heart that directly reflect its complex in vivo physiology. It has been widely used for the assessment of human heart diseases as well as in experimental heart disease models, as in mice. Compared to the human heart, the data acquisition from the mouse heart is more challenging for achieving adequate spatial and temporal resolutions. The mouse heart is about

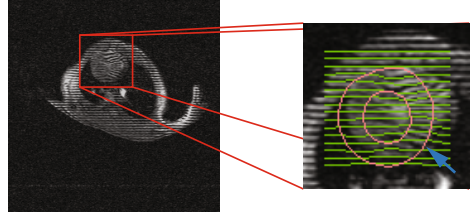


Fig. 1. Sample tagged SA image with tagging line tracking result

1000th the size of a human heart and beats much faster, at 400-600 beats per minute (bpm), than the human heart, with 60-80 bpm. Currently available MRI instruments for mouse imaging operate at a higher magnetic field strength (4.7T or above) than clinical MRI scanners, but they are still unable to provide temporal and spatial resolution in proportion with the mouse heart rate and size. Consequently, the tagging lines extracted from the mouse tMRI images contain more outliers than that from human data, as shown in Fig. 1.

MRI images are widely used for cardiac motion analysis [19]. In particular, the 3D characterization of the mouse cardiac mechanical function has been reported in [5,21,24]. However, all the prior methods assume that the tagging lines are manually labeled or correctly tracked. They cannot handle the tracking errors due to low image quality. To solve this problem, we employ our sparse deformable models to build an automatical strain analysis system based on tagged MRI images.

The system consists of four major components: 1) tagging line tracking, 2) control point tracking, 3) meshless model construction, and 4) meshless deformation. A Gabor filter bank [4] has been implemented to generate corresponding phase maps from low quality tagged MRI images. Then the 3D control points are tracked, based on the tagging lines and the contours of separate slices. The initial 3D meshless model of the end-diastole LV is built based on the sparse 2D contours [22]. First, a standard LV surface model, manually segmented from 3D CT data, is registered to the sample specified boundary using coherent point drift (CPD) [9]. Then a dense 3D point cloud is generated based on the fitted surface. When many LV surface samples are available, methods based on active shape models, like SPASM [2], are able to capture more model details. However, it is hard to collect enough training data in reality. Our method generate reasonable LV model with only one sample. Finally, the initial model is driven by the control points to track the LV movement along a cardiac cycle with our proposed sparse deformable model, and the motion strains are calculated locally based on the tracking result.

3 Experiments

3.1 Validations on Synthetic Data

We tested our sparse deformable models (SDM) on synthetic 3D volumes with known deformation. We first manually generated an LV volume model with the internal points evenly distributed on SA and LA directions. Twenty percent of SA slices with equal intervals were chosen as the control points. We then applied random global transformations, such as scaling, rotation and twisting, to the initial model. Two kinds of errors were applied to the deformed model to simulate the noisy tracking results. Gaussian noise was added to all control points, and a few points were selected randomly and large displacements were applied to them to simulate gross errors. Based on the displacements of the control points, we used the proposed sparse deformable models to reconstruct the displacements of the other points. The deformable models were tested under different parameters and different noise intensities. In each parameter setting, we randomly generated 1000 samples and calculated the mean and variance of deformation errors.

We first analyzed the relation between the deformation errors and the coefficient γ , reflecting the balance between the $L1$ and $L2$ norms (Fig. 2(a)). The sparse deformable models with both $L1$ and $L2$ norms were tested with different γ . The deformation error is large when γ is close to zero, and reduces dramatically when γ is a little larger. The combined norm is more like an $L1$ norm when γ is small. This may imply that SDM with the $L1$ norm alone cannot handle Gaussian error properly. As γ becomes even larger, the mean error increases again. It becomes stable when γ is large enough, and it is similar to the result using only the $L2$ norm. The results show that the sparse deformable models with combined norm outperform the other models that use only one type of norm. Theoretically, the model achieves the best result when the threshold γ is

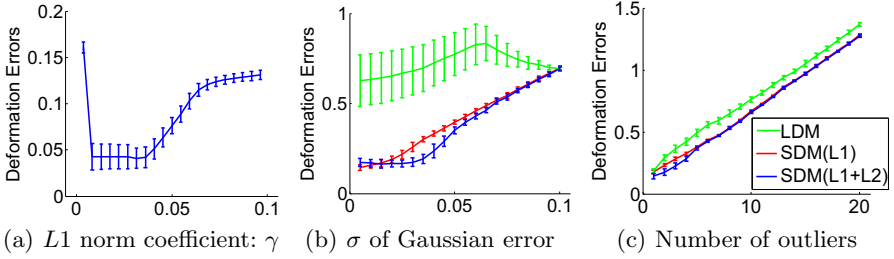


Fig. 2. (a) shows the deformation errors related to the coefficient γ of the $L1$ norm. (b) and (c) show the deformation errors of different deformable models. They are compared under different Gaussian noise variances and numbers of outliers, respectively. SDM with combined norm out-performs the other two most of the time, while SDM with the $L1$ norm is better when the Gaussian noise intensity is small.

similar to the variance of Gaussian noise. However, it is hard to measure the noise variance exactly in real data. We set it to one tenth of the median of the neighborhood distances empirically and the model shows good results.

We also tested our sparse deformable model under different noise intensities. First, we increased the variance of Gaussian noise with fixed outliers. In Fig. 2(b), SDM with $L1$ norm performs the best when the noise intensity is low. As the variance increases, SDM with combined norm out-performs the others. LDM is always the worst, due to the outliers. This experiment shows that our model is more stable with moderate Gaussian noise. Then we tested the models with different numbers of outliers. In Fig. 2(c), the errors of all models increase almost linearly with the number of outliers. SDM with combined norm, which is still the best among them, performs better than the SDM with $L1$ norm when there are a few outliers. They achieve similar errors when the outliers are dominant. Both of the experiments show that SDM with combined norm is more stable under different noisy conditions.

3.2 Left Ventricle Motion Analysis

We also tested our method on mouse myocardial strain analysis. The strain computation is especially sensitive to tracking outliers. Even when there are only a small amount of outliers on deformation, the strains on points near these outliers will be affected. To obtain ground truth, we manually labeled the tagging lines in each 2D image, and then used the tag motion to drive a 3D LV volume model based on finite element method (FEM). This method is accurate. However, manual labeling is a long and tedious task and FEM is not efficient. In this experiment, we used this method as reference, and compared our models using automatic tagging line tracking results that contain outliers. The results are compared between the LDM, SDM with only $L1$ norm and SDM with both $L1$

and $L2$ norms. Table 1 shows the deformation errors of different models on our 9 datasets. SDM with the combined norm has smaller average error than the others, owing to its robustness to outlier. Meanwhile, the results of SDM with $L1$ norm alone are much more unstable than other two methods. This may be because there is strong Gaussian noise in real data.

We also computed the myocardial strains over a cardiac cycle, which are commonly used to describe the strength of the heart motion. The strains are decomposed into radial, circumferential, and longitude directions, and the shear strains among them. Fig. 3 compares the strains generated with different deformable models on three mouse datasets. The

rows correspond to different types of strains, and the columns correspond to different mice. Each figure contains the strains generated from different models in a cardiac cycle. The numbers of frames in the cardiac cycles may be different on each mouse because of the acquisition procedures. The first column is from a normal mouse, and the other two are from mice with myocardial infarction. We observe that the strains generated from the healthy mouse are larger than from the unhealthy ones. For each individual dataset, the strains generated from the automatically tracked tagging lines are more unstable than those from manually labeled ones, due to the tracking errors. The strains based on LDM are relatively smooth, but this method tends to underestimate the strains. The results from SDM with the $L1$ norm have the largest instability. This may be because of its nature to pursue the sparse solution. Since the control points contain not only outliers, but also strong Gaussian noise, the $L1$ norm cannot handle Gaussian noise stably. The results from SDM with the combined norm best match the reference strains. This shows that our model performs well in the LV motion tracking based on inaccurate control points.

In order to analyze the local heart motion properties, we also visualize the strains on the external and internal surfaces of the left ventricle. Since the points of the surface mesh are all in the initial volume model, where the strains are calculated, we use them as samples and linearly interpolate the strains on the LV surface. The circumferential strains are shown locally on the LV external and internal surfaces in Fig. 4. They indicate larger contraction near the endocardium than near the epicardium. The high strain area begins near the apical endocardium and extends quickly toward the base, which is similar to human hearts.

Table 1. Quantitative evaluation of deformation errors (Unit: mm)

| Method | Average | Min | Max | Median |
|--------------|---------|-------|-------|--------|
| LDM | 1.036 | 0.724 | 1.635 | 0.927 |
| SDM, $L1$ | 2.107 | 0.437 | 3.580 | 2.069 |
| SDM, $L1+L2$ | 0.482 | 0.341 | 0.719 | 0.469 |

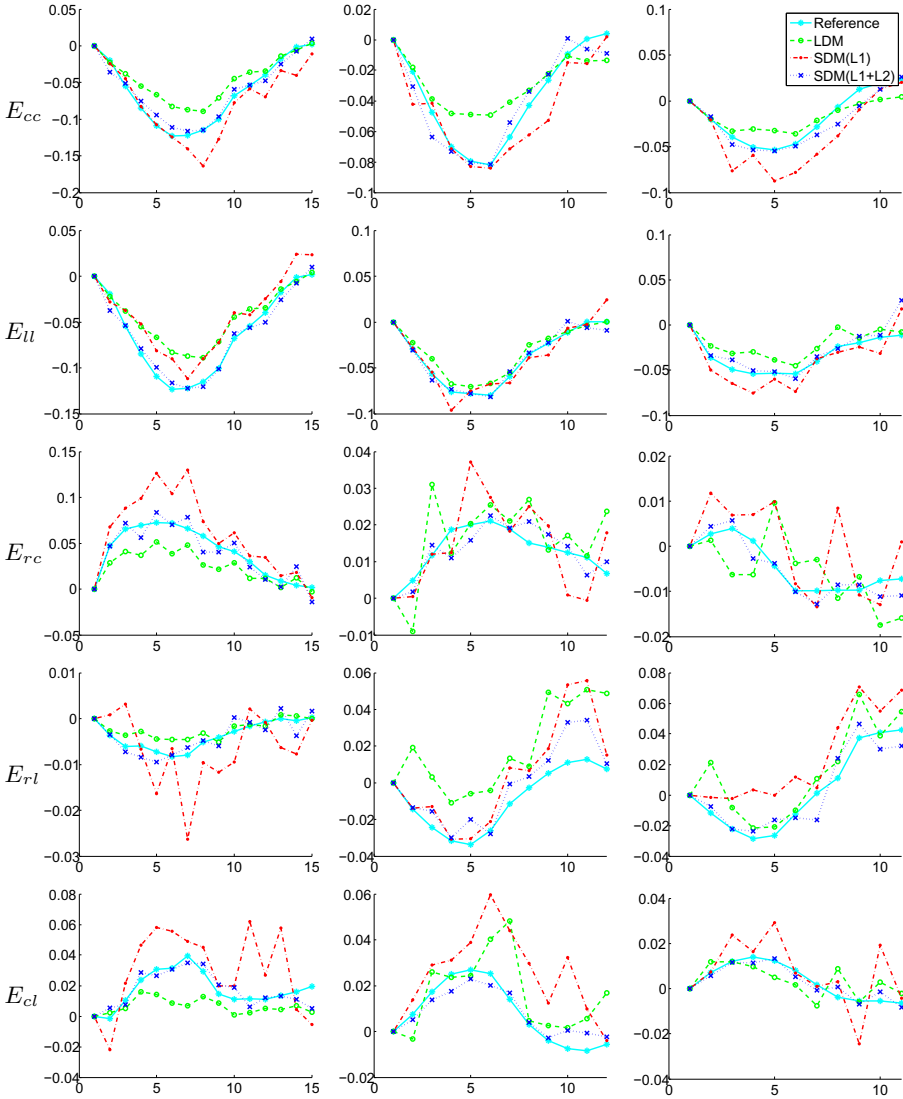


Fig. 3. Comparing the strains generated from different deformable models with the reference model in three mouse cardiac data. Each column represents one dataset, and each row represents one type of strain. In each figure, y-axis is the strain, and x-axis means the frame in a cardiac cycle.

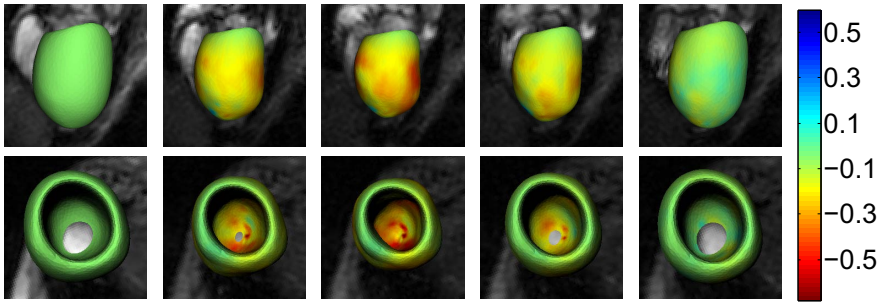


Fig. 4. The deformations of the left ventricle on a cardiac cycle are colored by the circumferential strain

4 Conclusions

In this paper, we introduce a group of sparse deformable models. Benefitted from the sparsity techniques, these deformable models are able to handle outliers or gross errors. Thus these models are robust when dealing with noisy images or tracking errors. We have validated these methods on both synthetic data and a cardiac motion tracking problem. Both qualitative and quantitative results demonstrate that our methods outperform and are more robust than previous ones. It is also noteworthy that the applications of our proposed methods are not limited to cardiac motion analysis. It is flexible enough for many other medical image problems.

In the future, we plan to extend the deformable models by using more constraints or priors. The left ventricle is conventionally separated into 17 segments. This inspires us to add group constraints to the current sparse model. The group sparsity and other structure sparsity constraints will further improve the robustness of the model. The current regularization term is only related to the external force based on noisy observations. It is easy to extend the other parts of the model. The problem for modeling arbitrary internal force is that the resulting model may not be a convex problem. The traditional finite difference method can be employed to find a local minimum, while the performance should then be further analyzed.

References

1. Amini, A., Chen, Y., Curwen, R., Mani, V., Sun, J.: Coupled B-snake grids and constrained thin-plate splines for analysis of 2-D tissue deformations from tagged MRI. *IEEE Transactions on Medical Imaging* 17(3), 344–356 (1998)
2. van Assen, H.C., Danilouchkine, M.G., Frangi, A.F., Ords, S., Westenberg, J.J., Reiber, J.H., Lelieveldt, B.P.: SPASM: A 3D-ASM for segmentation of sparse and arbitrarily oriented cardiac MRI data. *Medical Image Analysis* 10(2), 286–303 (2006)
3. Candes, E., Romberg, J., Tao, T.: Robust uncertainty principles: Exact signal reconstruction from highly incomplete frequency information. *IEEE Transactions on Information Theory* 52(2), 489–509 (2006)

4. Chen, T., Wang, X., Chung, S., Metaxas, D., Axel, L.: Automated 3D motion tracking using Gabor filter bank, robust point matching, and deformable models. *IEEE Transactions on Medical Imaging* 29(1), 1–11 (2010)
5. Chuang, J.S., Zemljic-Harpf, A., Ross, R.S., Frank, L.R., McCulloch, A.D., Omens, J.H.: Determination of three-dimensional ventricular strain distributions in gene-targeted mice using tagged MRI. *MRM* 64(5), 1281–1288 (2010)
6. Kass, M., Witkin, A., Terzopoulos, D.: Snakes: Active contour models. *International Journal of Computer Vision* 1(4), 321–331 (1988)
7. McInerney, T., Terzopoulos, D.: Deformable models in medical image analysis. In: *MMBIA*, pp. 171–180 (1996)
8. Metaxas, D.N.: *Physics-based deformable models: Applications to computer vision, graphics, and medical imaging*, 1st edn. Kluwer Academic Publishers (1996)
9. Myronenko, A., Song, X.: Point set registration: Coherent point drift. *IEEE Transactions on Pattern Analysis and Machine Intelligence* 32(12), 2262–2275 (2010)
10. Nealen, A., Müller, M., Keiser, R., Boxerman, E., Carlson, M.: Physically based deformable models in computer graphics. *Computer Graphics Forum* 25(4), 809–836 (2006)
11. Paragios, N., Deriche, R.: Geodesic active contours and level sets for the detection and tracking of moving objects. *TPAMI* 22(3), 266–280 (2000)
12. Radeva, P., Amini, A.A., Huang, J.: Deformable B-solids and implicit snakes for 3D localization and tracking of SPAMM MRI data. *Computer Vision and Image Understanding* 66(2), 163–178 (1997)
13. Shen, D., Davatzikos, C.: An adaptive-focus deformable model using statistical and geometric information. *TPAMI* 22(8), 906–913 (2000)
14. Shen, T., Huang, X., Li, H., Kim, E., Zhang, S., Huang, J.: A 3D Laplacian-driven parametric deformable model. In: *ICCV*, pp. 279–286 (2011)
15. Sorkine, O., Cohen-Or, D., Lipman, Y., Alexa, M., Rössl, C., Seidel, H.P.: Laplacian surface editing. In: *SPG*, pp. 175–184. *ACM* (2004)
16. Terzopoulos, D., Witkin, A., Kass, M.: Constraints on deformable models: Recovering 3D shape and nonrigid motion. *Artificial Intelligence* 36(1), 91–123 (1988)
17. Tustison, N., Amini, A.: Biventricular myocardial strains via nonrigid registration of AnFigatomical NURBS models. *IEEE Transactions on Medical Imaging* 25(1), 94–112 (2006)
18. Vogler, C., Goldenstein, S., Stolfi, J., Pavlovic, V., Metaxas, D.: Outlier rejection in high-dimensional deformable models. *IVC* 25(3), 274–284 (2007)
19. Wang, H., Amini, A.A.: Cardiac motion and deformation recovery from MRI: A review. *IEEE Transactions on Medical Imaging* 31(2), 487–503 (2012)
20. Wang, X., Chen, T., Zhang, S., Metaxas, D., Axel, L.: LV motion and strain computation from tMRI based on meshless deformable models. In: Metaxas, D., Axel, L., Fichtinger, G., Székely, G. (eds.) *MICCAI 2008, Part I. LNCS*, vol. 5241, pp. 636–644. Springer, Heidelberg (2008)
21. Young, A.A., French, B.A., Yang, Z., Cowan, B.R., Gilson, W.D., Berr, S.S., Kramer, C.M., Epstein, F.H.: Reperfused myocardial infarction in mice: 3D mapping of late gadolinium enhancement and strain. *JCMR* 8(5), 685–692 (2006)
22. Zhang, S., Wang, X., Metaxas, D., Chen, T., Axel, L.: Lv surface reconstruction from sparse tmri using laplacian surface deformation and optimization. In: *ISBI 2009*, pp. 698–701 (2009)
23. Zhang, S., Zhan, Y., Dewan, M., Huang, J., Metaxas, D.N., Zhou, X.S.: Towards robust and effective shape modeling: Sparse shape composition. *Medical Image Analysis* 16(1), 265–277 (2012)
24. Zhong, J., Liu, W., Yu, X.: Characterization of three-dimensional myocardial deformation in the mouse heart: An MR tagging study. *JMRI* 27(6), 1263–1270 (2008)